Modular and programmable material systems drawing from the architecture of skeletal muscle

Narayanan Kidambi, Ryan L. Harne, and Kon-Well Wang

Phys. Rev. E **98**, 043001 — Published 9 October 2018

DOI: 10.1103/PhysRevE.98.043001

Modular and programmable material systems drawing from the architecture of skeletal muscle

Narayanan Kidambi[1]*, Ryan L. Harne[2], and Kon-Well Wang[1]

[1]*Department of Mechanical Engineering, University of Michigan*

2350 Hayward St., Ann Arbor, MI, USA 48109

[2]*Department of Mechanical and Aerospace Engineering, The Ohio State University*

201 W 19th Ave., Columbus, OH, USA 43210

**Corresponding Author:*
Narayanan Kidambi
2350 Hayward St.
2223 GG Brown Building
Ann Arbor, MI
USA 48109
E-Mail: kidambi@umich.edu

Physical Review E section suggestions:

Solid Mechanics – Mechanical metamaterials

PhySH suggestions:

Elastic deformation

Conformation & topology

Abstract

The passive attributes of skeletal muscle "material" often have origins in nanoscale architecture and functionality where geometric frustrations directly influence macroscale mechanical properties. Drawing from concepts of the actomyosin network, this study investigates a modular, architected material system that leverages spatial constraints to generate multiple stable material topologies and to yield large adaptability of material mechanical properties. By exploiting the shearing actions induced on an actomyosin-inspired assembly of modular material constituents, new intriguing material behaviors are cultivated, including strong metastability and energy-releasing state transitions. Experimental, numerical, and analytical studies reveal that such passive attributes can be tailored by geometric constraints imposed on the modular material system. The geometric parameters can also introduce a bias to the deformations, enabling a programmable response. By invoking the spatial constraints and oblique, shear-like motions inherent to skeletal muscle architecture, this research illustrates new potential for architected material systems that exploit locally tunable properties to achieve targeted macroscopic behaviors.

1 Introduction and background

Skeletal muscle exhibits remarkable robustness, versatility, and adaptability. These attributes offer motivation to develop material systems that may emulate such characteristics. Many efforts in this spirit have sought to mimic whole-muscle morphology and behaviors, leading to significant progress in fields such as soft actuators [1–5], legged robotics [6–8], and electroactive polymers and hydrogels [9–12]. On the other hand, various advantageous characteristics of skeletal muscle have origins in the nanoscale constituents that comprise the actomyosin network [13]. The geometry, architecture, and functionality of these networks regulate the fundamental force-generating processes, robust and passive tension recovery, and a significant proportion of the strain energy storage in muscle [14–16]. Myocytes, the striated cells commonly called muscle fiber, consist of bundles of myofibrils that are sectioned into units called sarcomeres as shown in Figure 1(a-c). The length-tension responses of sarcomeres, the basic force generating unit of muscle, are strongly governed by the spacing between its adjacent thin and thick filaments [17]. Changes to this lattice spacing and overlap between adjacent filaments influences the ability of myosin heads to bind to sites along the actin filament, forming cross-bridges as depicted in Figure 1(d) [18]. For bound cross-bridges, the geometric constrains imposed by sarcomere length and lattice spacing affect the mechanics of the cross-bridge power stroke [17,19,20], in which the myosin head undergoes a rotation and conformational change due to adenosine triphosphate (ATP) hydrolysis. These constraints also influence the conformation changes that enable rapid passive tension recovery in consequence to sudden fiber length changes [21]. Furthermore, there is a strong interaction between axial contractile motions, transverse or radial forces, and elastic energy storage in skeletal muscle cross-bridges [15].

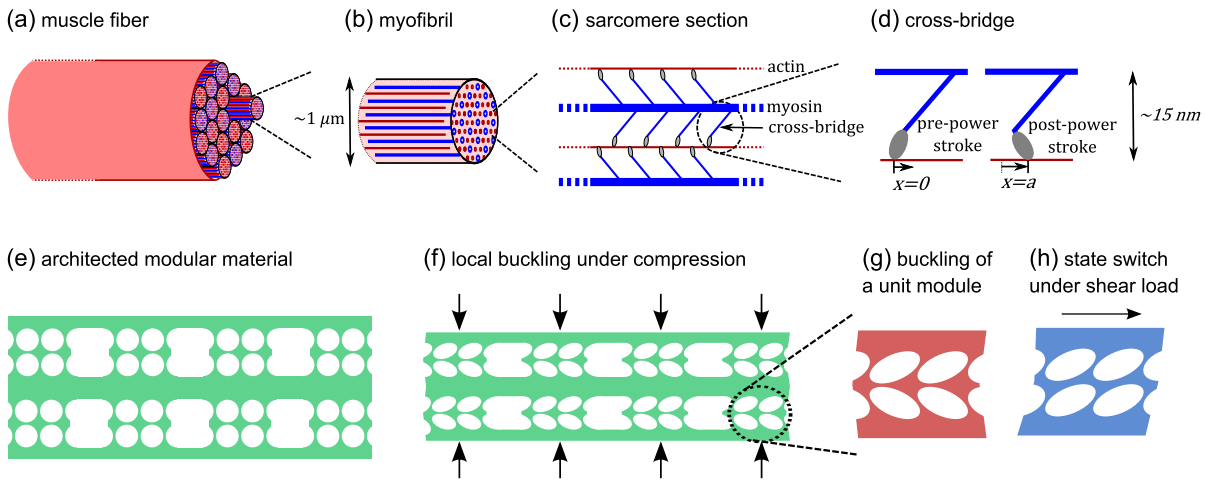

FIG 1. (a) Muscle fibers are composed of bundles of rod-like myofibrils (b), which consist of actin and myosin proteins arranged in a lattice and sectioned into units called sarcomeres (c). These filaments are connected by cross-bridges (d), with power stroke mechanics influenced by lattice geometry. (e) A section of proposed architected modular material system subject to compression (f), resulting in local buckling of constituent modules (g). Application of a shear load causes a state switch (h) in the void pattern.

Drawing from characteristics of the actomyosin networks in an effort to cultivate similar mechanical properties in material systems, the goal of this research is to explore and harness new architected materials that are inspired by skeletal muscle architecture. This is achieved by incorporating geometries that constrain the elastic energy storage elements in a manner functionally comparable to the confinement imposed on cross-bridges within the sarcomere sections. A schematic is presented in Figure 1(e-h) to illustrate the concept studied here. The architected material is composed of unit modules that each consist of four circular voids. The modules may buckle under sufficient transverse compression and undergo discrete state-switches when subjected to shear loads. The modules are separated by larger, rectangular voids that allow adjacent modules to express unique deformed topologies, reflecting the fact that within a sarcomere, adjacent cross-bridges may exhibit different conformations despite common lengths of the network [14,22]. In a simplified representation of the force-generating cross-bridge cycle [13,23], each attached cross-bridge exists in either a pre- or post-power stroke conformation. Thus, sarcomere contractile units may exhibit *metastability*, the coexistence of multiple combinations of cross-bridge conformations for a given sarcomere length where only one conformation is realized at a given time [14,24,25]. Transitions between these metastable configurations at different energy levels represent

the fundamental active force-generating actions in skeletal muscle, and have also been proposed as the origin for the remarkable ability of sarcomeres to rapidly and passively recover tension in consequence to sudden changes in length [14,26]. Such unique behavior has motivated recent study to consider muscle as a metamaterial, operating around points of instability that promote exceptional mechanical properties [14,25,27]. Past research on materials systems with patterned circular voids have revealed many intriguing behaviors, including the influence of void filling fraction and geometry on features such as negative Poisson's ratio and local buckling under tension and compression [28–30]. On the other hand, the material system proposed in this research learns from the cross-bridge conformational changes and the oblique, shearing motions between adjacent actin myosin filaments. This gives rise to new behaviors and properties previously unexplored, including strong metastability, and sudden transitions between locally stable configurations in consequence to oblique, shear motions.

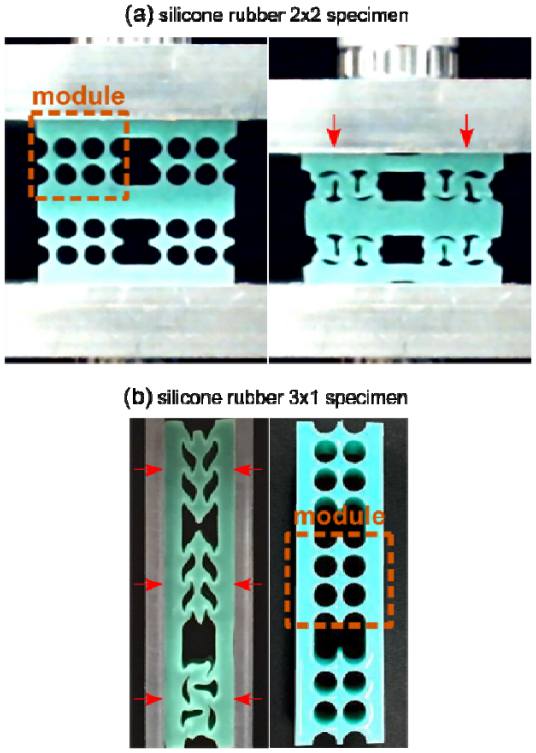

FIG 2. Architected material systems highlighting a four-void constituent module exhibiting local buckling under compression. (a) Two serially-connected sets of two modules in parallel. (b) Three-module system under transverse confinement, where each of the three modules exhibits a different deformation patterns despite being subject to the same confinement.

The existence of multiple equilibrium configurations of the modular constituents is noted in Figure 2. The images show undeformed and deformed topologies for material systems composed of (a) a 2x2 arrangement of modules, and (b) a 3x1 arrangement. A single four-void constituent module is highlighted for reference, and all modules are nominally identical. Details on material fabrication and testing are provided in the following Section 2. The two examples in Figure 2 illustrate how the architected material design incorporating sufficiently large rectangular voids between modules can lead to deformation patters that are localized to each module. Adjacent modules can hence possess qualitatively distinct topologies. Further, the 3x1 system clearly shows the existence of multiple statically stable equilibrium topologies for the same level of transverse compression. Hence, the architected material proposed in this research clearly gives rise to local metastability [14,22]. To gain a deep understanding of the unique mechanics afforded by the proposed material arrangement, comprehensive investigations are carried out on the four-void material module that may be assembled into new material systems in future studies.

The remainder of the paper is organized as follows. First, experimental and numerical analysis methods are introduced. Experimental results are presented for the mechanical response of a single four-void module under transverse confinement and shear motions in several metastable configurations. Numerical analysis reveals the origins of the sudden state-switching phenomena observed between certain metastable configurations and the influences of transverse confinement level. Then, the central segment of a module is modeled using elastica theory, offering insight into the effects of introducing a natural bias by varying the void geometry. The bias introduced by this non-uniform void geometry is studied experimentally and numerically, revealing the potential for programmable state-transition behaviors in multi-module sections of the proposed architected material system.

2 Experimental and numerical analysis methods

In this research, material specimens are fabricated from two-component silicone rubber mixture (Smooth-On Mold Star 15 SLOW [31]). The mixture is poured into molds fabricated using a stereolithographic 3D printer (Form 2, Formlabs Inc., USA), which employs a black photopolymer resin (GPBK02, Formlabs Inc., USA) at a 50μm print resolution. The molds are fabricated to reflect the complete geometry of the material, allowing the rubber to cure in the form of either a single module as in Figure 3(a), or as a system of multiple modules as in Figure 2, without the need for joints or adhesives between adjacent modules. The material is cured for four hours at 23 °C before being extracted from the molds and allowed to dry for at least 24 hours prior to testing.

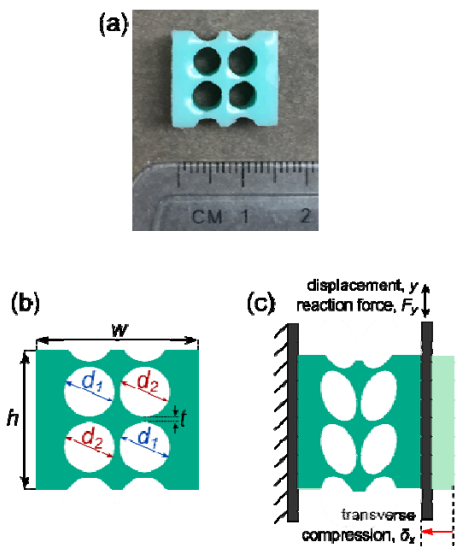

FIG 3. (a) Photo and (b) schematic of a unit module considered in this research, indicating important dimensions. (c) Transverse compression δ_x applied by aluminum plates. The plate on the left side is clamped to the base of a tensile testing machine, while the plate on the right side is clamped to the upper fixture and load cell.

A single module of the architected material system and its key geometric parameters are presented in Figure 3(a) and (b). The four voids have alternating diameters d_1 and d_2. All modules have height h = 15mm, width w = 15mm, wall thickness t = 0.88mm, and average void diameter ½(d_1+d_2) = 4.12mm. The center-to-center distance between adjacent voids is 5mm. These parameters are selected such that a unit module may buckle and the voids may collapse under a transverse compression [32]. A transverse

compression δ_x, as shown in Figure 3(c), is enforced by rigid aluminum plates clamped to the upper and lower fixtures of an Instron 5965 universal testing machine. Initial configurations are manually set by adjusting the module after it is placed in the test fixture. This is necessary to fully explore the range of displacements in which the various configurations are observed. Multiple tests are run for each starting configuration at a rate of 1mm/min. Since only elastic deformations occur, the material properties do not change with successive loading cycles and the material response is repeatable.

To supplement and guide experimental efforts, and provide a deeper understanding of state-switching behaviors in the architected material, numerical simulations are conducted using the ABAQUS software package (Dassault Systèmes Simulia Corp., USA). The Mold Star 15 SLOW silicone rubber material is modelled using a Neo-Hookean approximation. Young's modulus is obtained from a fit to experimental data for bulk material specimens, as shown in Figure 4. The compression puck and dumb-bell test specimens are dimensioned according to published ISO standards for determination of stress-strain properties [33,34]. The uniaxial Neo-Hookean stress-strain relationship for an incompressible material [35] is:

$$\sigma = 2C_1\left(\varepsilon + 1 - \frac{1}{(\varepsilon+1)^2}\right) \tag{1}$$

where C_1 is a material constant equal to *E/6* for the incompressible case, and σ and ε are the engineering stress and strain, respectively. The finite element model employs a nearly-incompressible Poisson's ratio to avoid numerical stability issues that would arise from a purely incompressible material with infinite bulk modulus [36]. The 2D domain is meshed with plane-strain six-node modified hybrid quadratic elements (element type CPE6MH). Under large transverse compression, complete collapse of the voids may cause the two surfaces of the material to contact each other. This behavior is incorporated in the finite element model by including a self-contact property, avoiding material interference.

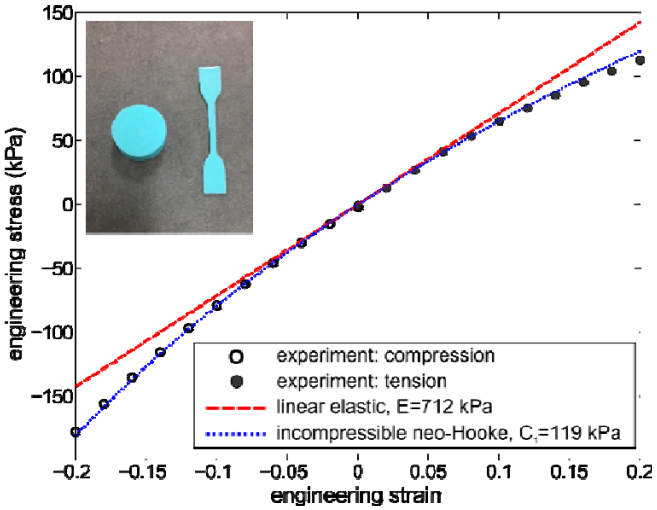

FIG 4. Stress-strain relationship of Mold Star 15 Slow silicone rubber from tension and compression tests. Linear-elastic and Neo-Hooke approximations are also presented. Inset: Bulk material specimens used in (left) compression and (right) tension tests.

Numerical analyses are conducted using the implicit ABAQUS/Standard solver. The left-most edge of the module is fixed in space while the right-most edge is vertical displaced as shown in Figure 3(c). Several combinations of transverse compression and vertical displacement paths are employed to reach the various configurations of a unit module. A small damping factor and slow displacement rates help enforce quasi-static conditions while capturing sudden state transitions. The force responses of interest are obtained by a summation of the vertical reaction forces (RF2) of the nodes at the boundaries of the elements of the element, while strain energy is extracted from the ALLSE variable.

3 Experimental results

As illustrated by the image shown in Figure 2, each module may exhibit one of many possible configurations for a given transverse confinement. Thus, to characterize these conformation in detail, cyclic loading is applied from the zero-displacement position under a variety of initial conditions. Figure 5 presents measurements of vertical reaction force, F_y, for a module with $d_1 = d_2 = 4.12$mm under cyclic loading up to vertical displacements of ± 6mm. Initial and final points are indicated by the hollow and filled circles, respectively, while arrows show the loading directions. In Figure 5(a), the initial, final, and intermediate deformed shapes of the module are characterized by the voids that point downwards,

resulting in a downward translation of the central vertical segment of the module with respect to the left and right edges. In Figure 5(b), the deformations are characterized by a symmetric configuration in which the voids are pointed in the upward direction. There is a large region of negative stiffness or negative slope around the zero-displacement position. Two positive stiffness regions are noted near the upper and lower limits of vertical displacement considered in these experiments. Due to symmetry of the module, mechanical responses of both configurations are similar.

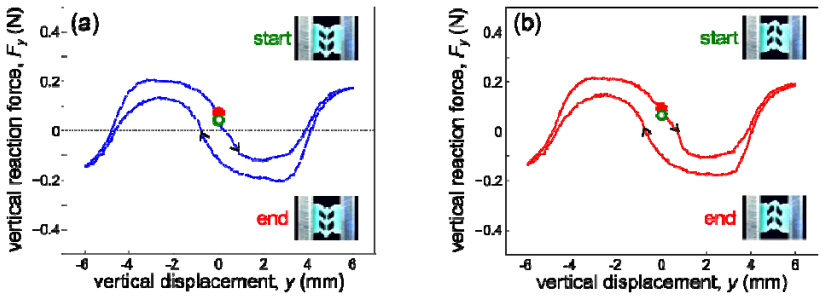

FIG 5. Force displacement results a full loading cycle when the module has an initial deformed configurations characterized by (a) voids pointed downwards and (b) voids pointed upwards.

When the initial configuration is characterized by voids that alternate between horizontally- and vertically-dominant shapes, half-cycle loading and unloading tests generate the responses presented in Figure 6(a-d). Half cycles are considered here since these response curves include a transition to the configurations shown in Figure 5, and hence completion of the full cycle would simply replicate a portion of the prior results. In Figure 6 (a) and (b) the initial states are prescribed such that the upper left void has a primarily vertical alignment. On the other hand, Figure 6 (c) and (d) present results from tests where the initial state is characterized a horizontal alignment of the upper left void. To probe the full extent of these configurations, loading cycles are initiated in both directions from the initial displacement. The segments of these tests highlighted by thick dotted and dash-dotted curves represent the portions in which the module retains the starting configuration. These segments are later aggregated (in Figure 7 and Figure 12) to show comprehensive force response results under all observed configurations. Portions of the responses indicated by the thin black curves thus correspond to segments where the configurations are the same as

in Figure 5, and are excluded from aggregated results. Rapid state transitions from the initial configuration are indicated by vertical segments of the force response.

The final configurations of the half-cycle experiments presented in Figure 6(a-d) all have voids oriented either downwards or upwards. To understand how load-displacement responses may evolve following a state transition, two examples are presented. Figure 6(e) presents one and a half cycles with the same initial configuration and displacement direction as depicted in 6(c). Following a transition to the configuration characterized by voids that are pointed downwards, the subsequent full cycle follows the trajectory of the complete cycle shown in Figure 5(a). On the other hand, Figure 6(f) presents a half cycle initiated from the end condition of the response shown in 6(d), and follows a portion of the trajectory depicted in Figure 5(b) for the configuration with voids pointed upward.

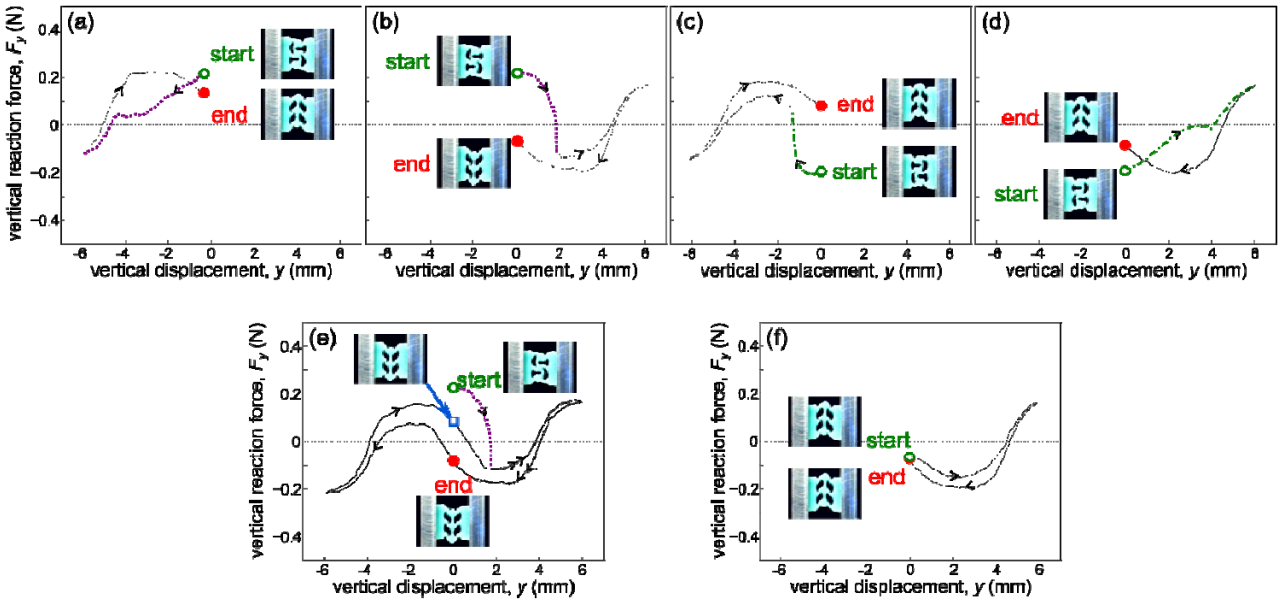

FIG 6. Responses from compression and extension tests where the initial configuration is characterized the upper left void deformed such that it is extended (a,b) vertically and (c,d) horizontally. The thick curve segments represent the portions in which the module retains the starting configuration, while the thin segments denote portions following a transition to one of the states shown in Figure FIG 5. (e) A half-cycle with the same starting conditions as in (c) followed immediately by a full cycle. This indicates that following a transition to one of the states in Figure 5, subsequent loading cycles remain in that configuration. (f) A half-cycle repeated from the end condition of (d).

4 Influence of transverse confinement on material response

4.1 Aggregated experimental results

In skeletal muscle, inter-filament lattice spacing affects the forces and energy storage of myofilaments and cross-bridges. Similarly, the geometric confinements imposed by transverse compression in the architected material studied here has a strong influence on its mechanical response. Aggregated measurements of vertical reaction force, F_y, for a module with void diameters $d_1 = d_2 =$ 4.12mm are presented in Figure 7(a-d) for four different levels of transverse compression δ_x/w. In order to capture the full extent of the observed topologies, responses from several loading cycles with various starting configurations are combined in each plot.

Reaction force magnitudes are greater as δ_x is increased, which is intuitive based on larger local stresses associated with greater transverse compressions. Further, increased transverse compression results in larger hysteresis. The hysteresis is likely due to the onset of self-contact and friction as the voids collapse when subjected to the increased confinement, as suggested by the figure insets. The four curves (solid, dashed, dotted, and dash-dotted) denote different deformed shapes, corresponding to the segments of the same line styles shown in Figure 5 and Figure 6. The shaded regions around the zero-displacement positions highlight the range of displacements for which all four configurations are observed. This region is termed the *highly metastable range*, and the polygon labels in Figure 7(c) correspond to the distinct metastable states shown Figure 7(e,f) for $\delta_x/w = 0.13$. Configurations are classified in two types according to the nature of the deformations. *Aligned* topologies are shown by solid and dashed curves, and denote deformations of the voids that are all aligned in the same direction. *Polarized* topologies, indicated by dotted and dash-dotted curves, are characterized by a rotation of the central segment, causing void deformations to alternate between horizontally- and vertically- dominant shapes. The highly metastable range is absent the lowest level of transverse compression $\delta_x/w = 0.10$, shown in Figure 7(a), since no polarized topologies are observed.

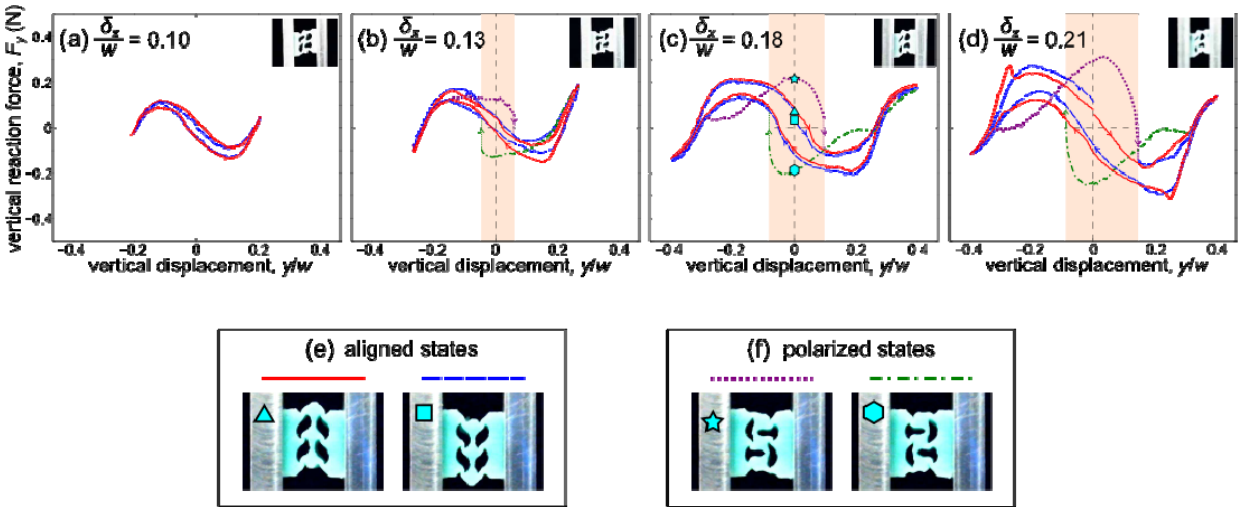

FIG 7. (a-d) Experimentally-measured vertical reaction force-displacement responses for four levels of transverse compression δ_x/w for a module with $d_1 = d_2 = 4.12$ mm. Thin vertical dotted lines marked with arrows at the boundaries of the shaded *strongly metastable range* indicate discrete state transitions. Line styles correspond to the aligned and polarized topologies presented in (e) and (f). The polarized topologies are not observed for the lowest level of transverse compression.

The highly metastable ranges provide an opportunity to dramatically adapt stiffness and reaction force by switching between topologies while boundary conditions remain unchanged. Reaction force responses of the aligned configurations are characteristic of a bistable element, with a locally negative slope (i.e. negative stiffness) for a region surrounding vertical displacement $y = 0$, and positive slope or stiffness outside this region. On the other hand, the polarized states exhibit near-zero stiffness in the highly metastable range for $\delta_x/w = 0.13$ and greater stiffness as transverse compression is increased. The shaded metastable regions in Figure 7(a-c) are bounded by vertical dotted lines marked with arrows indicating observed polarized-to-aligned state transitions, which cross the horizontal axis and result in sudden changes to stiffness and reaction force magnitude and direction (See Supplemental Video S1 [37])

4.2 Numerical analysis results

Finite element analyses establish a deeper understanding of these state-switching behaviors. In a procedure similar to the one pursued for the experimental investigations, cyclic simulations with slowly varying boundary conditions are undertaken from various starting positions. The aggregated results of reaction force are presented in Figure 8(a-d) showing trends that are comparable with the experimental

results in Figure 7. A minimum transverse compression level is required before the shaded highly metastable range appears, and increased compression levels lead to larger reaction force magnitudes. The points highlighted in Figure 8(c,i) correspond to the aligned an polarized topologies in Figure 8(e,f), which are equivalent to the experimental topologies presented in Figure 7(e,f). Crucially, finite element simulations facilitate an examination of system energies, which is not possible directly from the experimental force response results in the presence of sudden, dissipative state transitions [38]. Figure 8(g-j) presents strain energies plotted on the same scale, revealing that strain energy levels increase with transverse compression. Such a relationship between transverse confinement and strain energy level may be anticipated since greater transverse compressions must be accommodated by larger deformations and increased local stresses. For a transverse compression of $\delta_x/w = 0.21$, the maximum principal stresses in the aligned topologies depicted in Figure 8(e) are 2.6 times greater than for $\delta_x/w = 0.10$. Further, numerical results reveal that the polarized configurations are at a higher energy level than the aligned topologies, and that polarized-to-aligned transitions are enabled by rapid releases of strain energy. The quantity of energy released in consequence to these transitions also increases with transverse compression.

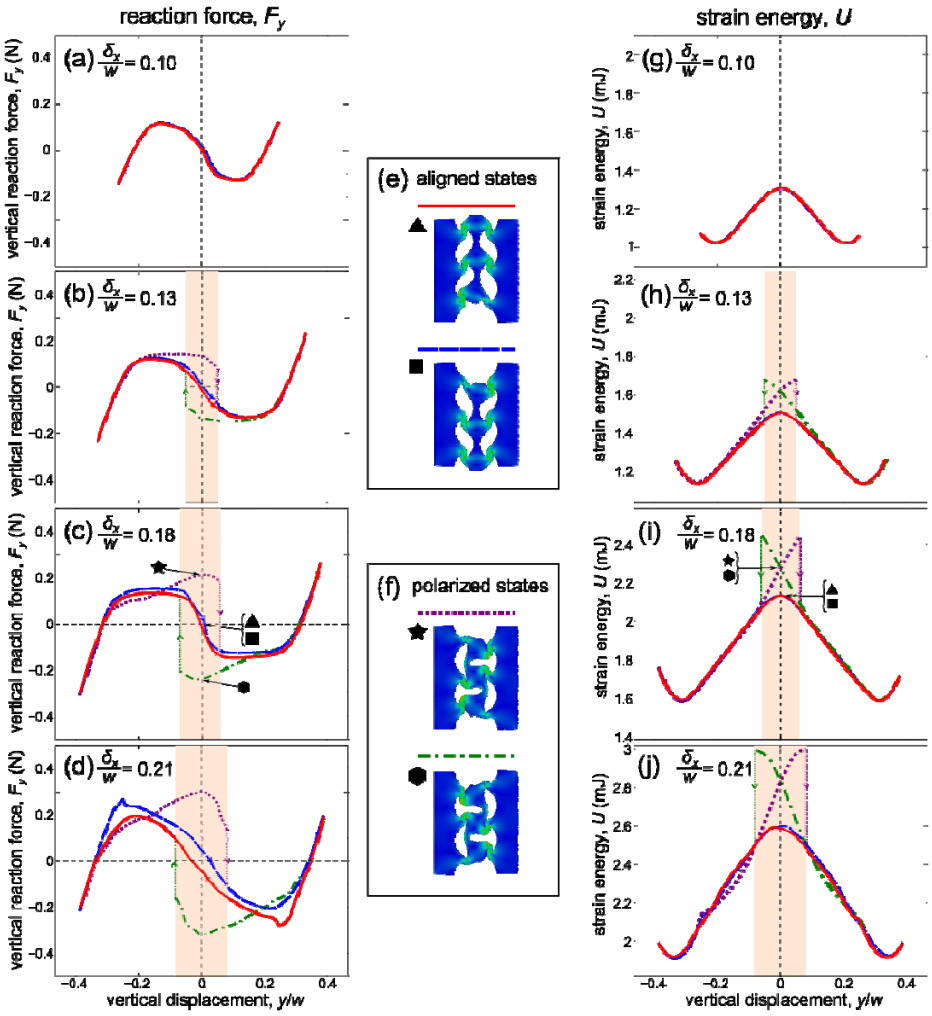

FIG 8. Numerical results of a module with uniform void geometry subject to oblique displacements under four different levels of transverse compression. (a-d) Trends in reaction force responses show reasonable agreement with the experimental results shown in Figure 7(a-d). (g-j) Strain energy curves reveal the large strain energies stored in the polarized states within the shaded highly metastable regions. (e,f) Images showing aligned and polarized topologies as predicted by the finite element model, with line styles corresponding to the curves in (a-d, g-j).

Both experimental and numerical investigations illustrate that as transverse confinements and vertical displacements of a material module are changed, there is variation in the number of available metastable configurations. This behavior shares some similarities with the recruitment of cross-bridges in activated muscle. For sarcomeres extended far beyond the natural length, there is reduced overlap between adjacent actin and myosin filaments, which reduces the likelihood of cross-bridge formation [18] and hence the number of metastable configurations. The reduction in the number of cross-bridges available for recruitment also compromises the maximum possible active forces that sarcomeres can generate. For

sarcomere lengths much less than the natural elongation, thin filaments may overlap, and the radial distance between the thick filament and thin filament increases [13,18]. This can similarly compromise cross-bridge formation.

5 Influence of module geometry on material response

5.1 Analytical approximation using Euler's elastica

Finite element numerical analysis demonstrates good agreement with experimental results and offers deeper insight into the strains and energies of the material module under various conditions. However, this approach is computationally expensive and requires careful tuning of initial conditions to capture the various configurations. To overcome these obstacles and shed light on the module mechanics, an analytical model is developed. This model is then employed to facilitate study on the influence of module geometry on the fundamental mechanical response.

Examination of the central horizontal member of a single module under transverse confinement, as shown in Figure 9(a), suggests that the deformation of this member may be approximated by large-scale deformations of a flexible beam clamped at both ends. Hence, elastic curve solutions are developed for the parameters and boundary conditions described in Figure 9(b). A flexible beam with length L, Young's modulus E, second moment of inertia I, is clamped at both ends at an angle β with respect to the horizontal. The two clamped ends are separated by a horizontal distance of L-δ_x and a vertical distance of y_e, respectively. Here, the method developed by Shoup and McLarnan [39,40] is adopted. Further details are presented in the appendix. The five equations that result from this formulation are solved using the built-in MATLAB function *fsolve* to yield solutions for the five unknowns. Since multiple solutions are possible and *fsolve* employs iterative methods, suitable initial estimates must be provided. These initial guesses are selected based on the desired number of inflection points and concavities at the clamped ends [40] corresponding to the aligned and polarized topologies presented in Figure 9(a).

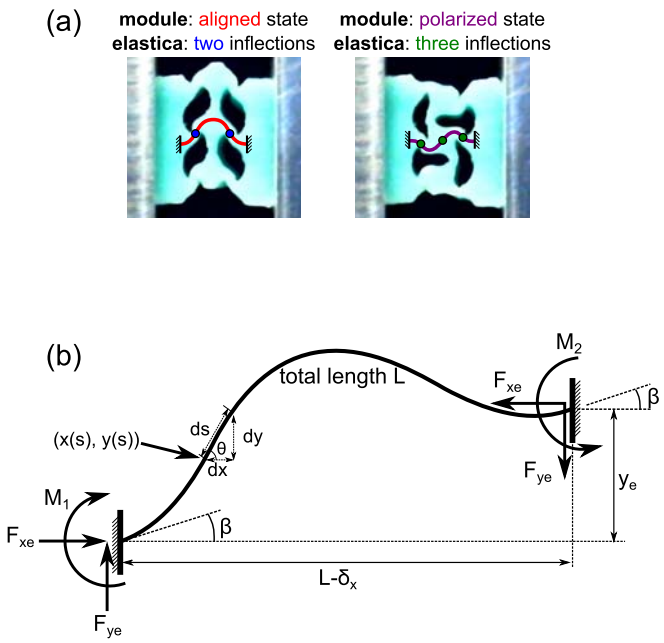

FIG 9. (a) Module highlighting deformations of central horizontal member in polarized and aligned deformed topologies. (b) Schematic of a flexible beam with boundaries clamped at an angle *β*.

Nondimensionalized vertical reaction force and strain energy plots of the elastica model are presented in Figure 10(a-c) and (d-f), respectively, showing solutions with different numbers of inflection points. The assumption of inextensibility in the elastica model and the absence of intersecting vertical members leads to an over-prediction of the range in which polarized (three-inflection) states are observed. Nevertheless, key features are captured. Force responses show a clear negative stiffness region for the two-inflection solutions that represent the aligned topologies. Further, elastic curve solutions with three inflection points, which are an analogue to the polarized states of the module, are at a higher strain energy level than the two-inflection solutions. A bias is introduced to the model by prescribing a nonzero clamp angle β at both ends, which predisposes the beam towards certain elastic curve solutions. The influence of this bias is noted, and the difference between the strain energies of the three-inflection solutions grows as the clamp angle is increased. The elastica approximation may thus be developed as part of a design tool for the development of architected material systems composed of large numbers of modules with varying geometry.

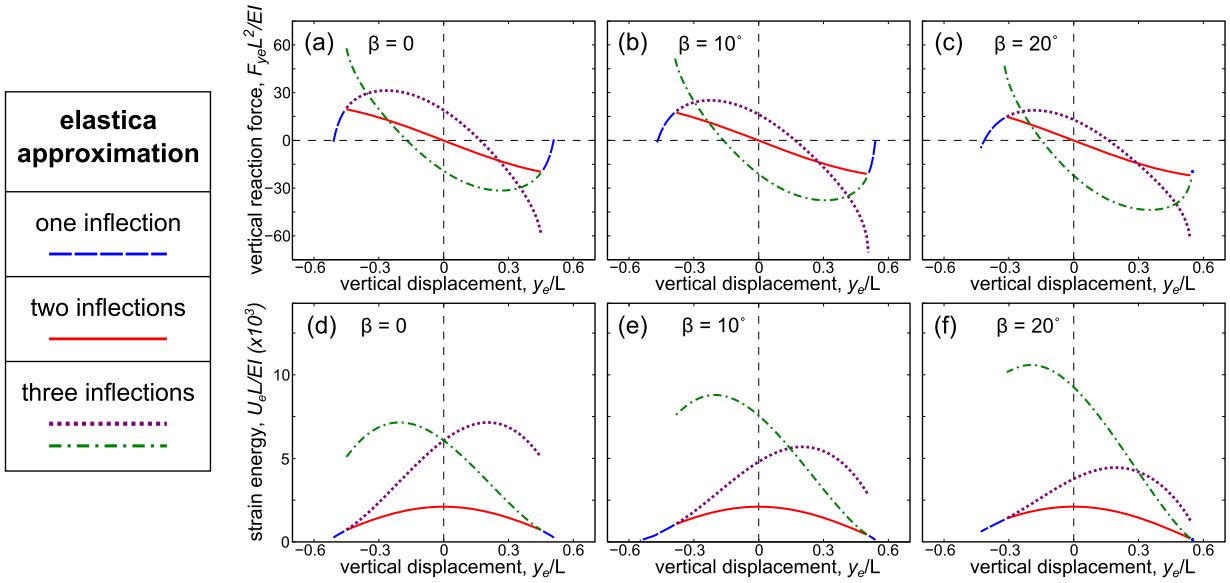

FIG 10. Nondimensionalized (a-c) reaction force and (d-f) strain energy for the clamped elastica, with bias reflected by introducing a nonzero clamp angle *β*. Numerical results and the elastica model show that the polarized or three-inflection states are at higher strain energy levels than the aligned or two-inflection states

5.2 Introduction of bias through variation of void diameters

The elastica approximation of Figure 10 reveals the effect of introducing a bias by varying the boundary clamp angles. This may be reflected in the architected material by considering elements with non-uniform void geometry, as depicted in Figure 11. Void diameters d_1 and d_2 are varied, while the wall thickness t separating the voids remains fixed at t = 0.88mm. To understand the influence of void geometry on material response and to verify the predictions offered by the elastica approximation, thorough experimental and numerical studies are conducted.

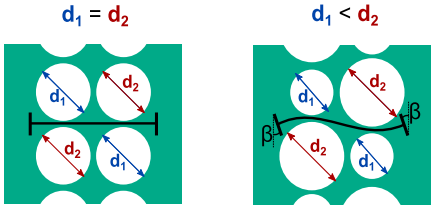

FIG 11. Illustration of a module with non-uniform void diameters and approximation of this geometry with nonzero clamp angle *β* of the flexible beam.

Figure 12(a-c) presents vertical reaction force responses obtained from experiments on modules with (a) $d_1 = d_2$, (b) $d_1 = 0.94 d_2$, and (c) $d_1 = 0.89 d_2$. Corresponding strain energies calculated from finite element analyses are shown in Figure 12(d-f). As the difference between diameters d_1 and d_2 grows, polarized states marked by dotted curves are observed for a larger range of vertical displacements, and are generally at a lower strain energy than those marked by dash-dotted curves. The polarized states are biased towards topologies characterized by vertically dominated deformed shapes of the smaller voids, just as the three-inflection elastica curves are biased in presence of a nonzero clamp angle. This asymmetry also influences the location and extent of the shaded highly metastable range. As the level of bias is increased, these metastable regions move towards more positive vertical displacements. As a result, the locations of the sudden polarized-to-aligned state transitions are modulated. This suggests an opportunity to tune the response of these modular constituents by strategic selection of void geometries.

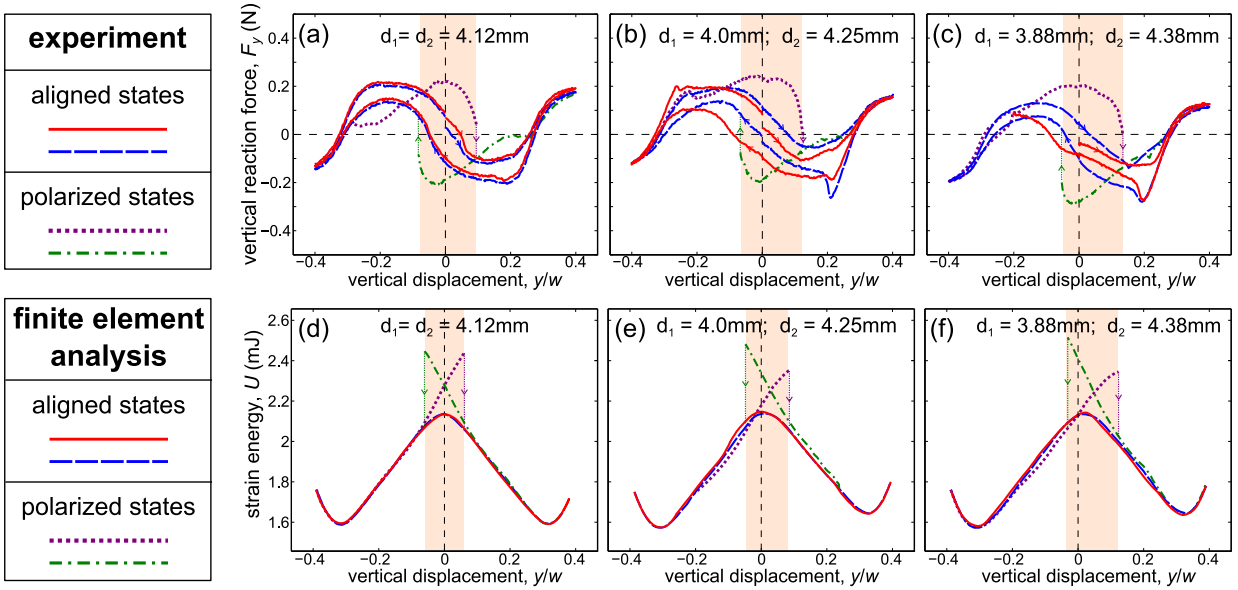

FIG 12. Force and energy responses of modules with non-uniform void diameters. (a-c) Experimental results showing vertical reaction force-displacement responses and (d-f) numerical results showing strain energies as void diameters d_1 and d_2 are varied, demonstrating a bias towards one of the polarized states as the difference between d_1 and d_2 increases.

The arrangement of several modules with varying void geometry provides a means to program the mechanical response by prescribing the order in which these transitions will occur. The fabrication of specimens composed of multiple modules follows the procedure described in Section 2, with molds

fabricated using a 3D printer to reflect the complete geometry of the specimen. Hence, larger, multi-module specimens such as those presented in Figures 2 and 13 cure as a uniform section of the Mold Star 15 silicone rubber. This avoids the need to employ fasteners or adhesives to join together individual modules. Large, rectangular voids separating adjacent modules allows each to deform independently. Hence, the mechanical response of a parallel arrangement of modules can be described by the superposition of single-module responses. Since one module exhibits up to four qualitatively distinct topologies, a parallel arrangement of n modules will have 4^n possible configurations. As an example, Figure 13(a) depicts the 16 metastable configurations of a two-module specimen. The results of Figure 13(b) illustrate how a system composed of three modules with different void geometries can yield programmable behavior under transverse compression. The uppermost module has diameters $d_1 = d_2$, the central module has $d_1 = 0.9d_2$, and the lower module has $d_1 = 0.8d_2$. All three are initially in the polarized configuration characterized by a vertical alignment of the upper left void. However, due to the varying bias introduced by the void geometry, and according to the trends described in Figure 12, the polarized states suddenly transition to aligned topologies at three different levels of shear displacement. First, the lower module, which has the greatest bias or asymmetry, undergoes the state switch. This is followed by the central module, then by the symmetric module at the top of the material section. Results from three experiments are presented, indicating repeatability of the observed phenomena. Images show the combinations of configurations that are observed in each shaded region.

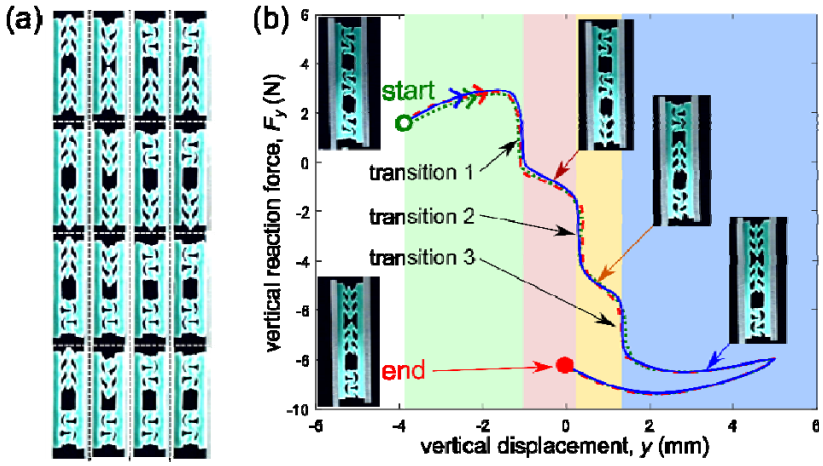

FIG 13. (Color online) Multi-module specimens. (a) The 16 possible metastable configurations for a material section composed of two modules. (b) Programmable response in an arrangement of modules with different void geometries. The upper modules has $d_1 = d_2$, the central module has $d_1 = 0.9d_2$, while the lower module has $d_1 = 0.8d_2$. If the initial configuration is such that all three modules are the polarized state characterized by a vertical shape of the upper left void, prescribing shear motions will result in different thresholds for which sudden polarized-to-aligned transitions occur. These transitions are indicated by vertical jumps in reaction force. Results from three trials are presented, indicating repeatability.

Consideration of a section the proposed architected material composed of several modules in parallel would greatly enhance the programmable behavior and force or stiffness adaptivity, since their combined response would arise from a superposition of the individual module responses [22]. The availability of multiple coexistent metastable configurations, and the programmable state transitions between them, may be useful in applications that call for robust shape change and properties adaptivity including soft robots and actuators. By embedding the intelligence of the system within its structure and geometry, the need for complex feedback controls is reduced [11,41]. Further investigation of ways in which discrete configuration changes can be used to generate programmable movements and motions of soft material systems could foster the development of adaptable soft robotic systems. In order to actively generate these configuration changes, several actuation methods may be explored, including pneumatic or fluidic methods [42,43] or using incorporating ferromagnetic elements that may cause targeted portions of the material system to react to changes in externally-applied magnetic fields [44].

6 Conclusions

Drawing from the architecture of skeletal muscle constituents, this research investigates a novel architected material offering intriguing behaviors not revealed by previous work. Geometrically-constrained local conformation changes in sarcomeres and cross-bridges, which are the origin for macroscopic force-generation and length change in muscle, serve as motivation to investigate the mechanical response of constrained modular material systems. Multiple *metastable* configurations are uncovered for prescribed boundary conditions, demonstrating means to drastically adapt mechanical properties and stored strain energy in the material system. Oblique, shear-like loads, representative of the sliding motions between adjacent actin and myosin filaments during sarcomere length change, give rise to energy-releasing state transitions that cause dramatic changes in reaction force and stiffness. Comprehensive experimental, numerical, and analytical studies are undertaken, revealing the influence of transverse confinements on the material response. A model of module deformations is developed using Euler's elastica, allowing for valuable insight to be obtained from a simplified analogue of the complex architected material behavior. Asymmetry is introduced by varying the boundary conditions in the elastica model, which corresponds to varying the void diameters in the material system. This causes a bias towards certain configurations and influences the range in which the metastable configurations may be observed and allows for a programmable response of a system composed of multiple modular constituents. By learning from the micro- and nanoscale morphology of skeletal muscle, this research introduces a material architecture with the potential to achieve new mechanical properties and functionalities in systems that call for greatly enhanced versatility and adaptability.

Acknowledgements

This research is supported by the U.S. Army Research Office under grant number W911NF-15-1-0114, with Dr. Samuel C. Stanton as the Program Manager.

Appendix

This section presents a solution to the elastica curves approximating the deformation of the central horizontal member of a single module, and an expression for the bending strain energy stored in the beam. The method developed by Shoup and McLarnan [40] is adopted here.

The curvature of an Euler-Bernoulli beam at any arbitrary point along the beam is described by [40,45]:

$$EI\frac{d\theta}{ds} = M(s) \tag{A-1}$$

where E is the Young's modulus, I is the area moment of inertia, and $M(s)$ is moment required for static equilibrium at $(x(s),y(s))$. Equating moments about this arbitrary point and differentiating with respect to $\boldsymbol{s}$ yields:

$$EI\frac{d\theta}{ds} = M_1 - F_{xe}y + F_{ye}x \tag{A-2}$$

$$EI\frac{d^2\theta}{ds^2} = -F_{xe}\frac{dy}{ds} + F_{ye}\frac{dx}{ds} \tag{A-3}$$

Noting that $\frac{dy}{ds} = \sin(\theta)$ and $\frac{dx}{ds} = \cos(\theta)$, the overall length of the elastica and the geometry of the boundary points can be expressed as:

$$\int_0^{S^*} ds = L \tag{A-4a}$$

$$\int_0^{S^*} \cos(\theta)ds = L - \delta_x \tag{A-4b}$$

$$\int_0^{S^*} \sin(\theta)ds = y_e \tag{A-4c}$$

In order to make use of these conditions, Eq. (A-3) is first rewritten and integrated with respect to θ.

$$\int EI\frac{d^2\theta}{ds^2}d\theta = -F_{xe}\int \sin(\theta)d\theta + F_{ye}\int \cos(\theta)d\theta \tag{A-5}$$

$$\frac{1}{2}E\left(\frac{d\theta}{ds}\right)^2 = F_{xe}\cos(\theta) + F_{ye}\sin(\theta) + Z \tag{A-6}$$

where Z is a constant of integration. Rearranging gives:

$$ds = \left(\frac{EI}{2(F_{xe}\cos(\theta) + F_{ye}\sin(\theta) + Z)} \right)^{\frac{1}{2}} d\theta \tag{A-7}$$

Eq. (A-7) can be substituted into Eq. (A-4), however the expressions cannot be integrated across points of inflection ($\frac{d\theta}{ds} = 0$) [46]. This is addressed by introducing new parameters that allow equations (A-4a-c) to be expressed using elliptic integrals [40,47].

$$P\cos(\alpha) = \frac{2F_{xe}}{EI} \tag{A-8a}$$

$$P\sin(\alpha) = \frac{2F_{ye}}{EI} \tag{A-8b}$$

$$C = \frac{2Z}{EI} \tag{A-8c}$$

which can be combined with basic trigonometric identities giving:

$$ds = \left(\frac{1}{P\cos(\alpha)\cos(\theta) + P\sin(\alpha)\sin(\theta) + C} \right)^{\frac{1}{2}} d\theta$$

$$ds = \left(\frac{1}{P(\alpha - \theta) + C} \right)^{\frac{1}{2}} d\theta$$

Further, a change in the variable of integration is facilitated by the following transformations:

$$2k^2 = \frac{C}{P} + 1 \tag{A-9a}$$

$$1 - 2k^2\sin^2(\phi) = \cos(\alpha - \theta) \tag{A-9b}$$

Differentiating and rearranging (A-9b) by using trigonometric identities yields:

$$d\theta = 2k\cos(\phi)\left(1 - k^2\sin^2(\phi)\right)^{-\frac{1}{2}} d\phi \tag{A-10a}$$

and:

$$\sin(\theta) = \sin(\alpha)\left(1 - 2k^2\sin^2(\phi)\right) + \cos(\alpha)\left(2k\sin(\phi)\right)\left(1 - k^2\sin^2(\phi)\right)^{\frac{1}{2}} \tag{A-10b}$$

$$\cos(\theta) = \cos(\alpha)\left(1 - 2k^2 \sin^2(\phi)\right) - \sin(\alpha)\left(2k \sin(\phi)\right)\left(1 - k^2 \sin^2(\phi)\right)^{\frac{1}{2}} \tag{A-10c}$$

To allow integration using the new variables introduced in Eq. (A-9), the following elliptic integrals are employed [46]:

$$F_e(\phi, k) = \int_0^{\phi} \left(1 - k^2 \sin^2(\phi)\right)^{-\frac{1}{2}} d\phi \tag{A-11a}$$

$$E_e(\phi, k) = \int_0^{\phi} \left(1 - k^2 \sin^2(\phi)\right)^{\frac{1}{2}} d\phi \tag{A-11b}$$

$F_e(\phi,k)$ and $E_e(\phi,k)$ are the incomplete elliptic integrals of the first and second kind, respectively. These elliptic integrals are combined with Equations (A-6) and (A-10) to rewrite (A-7).

$$L = \left(\frac{2}{P}\right)^{\frac{1}{2}} \left(F_e(\phi_2, k) - F_e(\phi_1, k)\right) \tag{A-12a}$$

$$L - \delta_x = \left(\frac{2}{P}\right)^{\frac{1}{2}} \left[\cos(\alpha)\left(-F_e(\phi_2,k) + F_e(\phi_1,k) + 2E_e(\phi_2,k) - 2E_e(\phi_1,k)\right) + 2k\sin(\alpha)\left(\cos(\phi_2) - \cos(\phi_1)\right)\right] \tag{A-12b}$$

$$y_e = \left(\frac{2}{P}\right)^{\frac{1}{2}} \left[\sin(\alpha)\left(-F_e(\phi_2,k) + F_e(\phi_1,k) + 2E_e(\phi_2,k) - 2E_e(\phi_1,k)\right) + 2k\cos(\alpha)\left(-\cos(\phi_2) + \cos(\phi_1)\right)\right] \tag{A-12c}$$

In Eqs. (A-12a-c), ϕ_1 and ϕ_2 are amplitudes corresponding to the left and right ends of the flexible beam respectively. Since $\theta(s=0) = \beta = \theta(s=L)$ is prescribed at the ends ϕ_1 and ϕ_2 may be found by solving (A-10b at both ends):

$$\sin(\beta) = \sin(\alpha)\left(1 - 2k^2 \sin^2(\phi_1)\right) + \cos(\alpha)\left(2k \sin(\phi_1)\right)\left(1 - k^2 \sin^2(\phi_1)\right)^{\frac{1}{2}} \tag{A-12d}$$

$$\sin(\beta) = \sin(\alpha)\left(1 - 2k^2 \sin^2(\phi_2)\right) + \cos(\alpha)\left(2k \sin(\phi_2)\right)\left(1 - k^2 \sin^2(\phi_2)\right)^{\frac{1}{2}} \tag{A-12e}$$

Eqs. (A-12a-e) are solved using the built-in MATLAB function fsolve to yield solutions for ϕ_1, ϕ_2, *k, P,* and α. Since fsolve employs iterative solvers, suitable initial estimates must be provided. Noting that points of inflection occur for $\phi = n\pi + \frac{\pi}{2}$ for $n \in \mathbb{Z}$, appropriate initial guesses for ϕ_1 and ϕ_2 are

employed to obtain elastica curves with the desired number of inflection points along the beam and concavities at the clamped ends [40], corresponding to the aligned and polarized topologies. Symmetry is used to solve for opposite concavities and boundary conditions.

Following the same approach as above, appropriate changes of variable and manipulations can be applied to the expression for bending strain energy. This allows the energy to be computed directly from the solutions to (A-12a-e).

First, the bending strain energy in an infinitesimal segment is integrated over the beam length [45]:

$$U = \int_0^{s^*} \frac{EI}{2}\left(\frac{d\theta}{ds}\right)^2 ds \tag{A-13}$$

Using (A-6) - (A-8) to change the variable of integration, this can be rewritten as:

$$U = \int\left(\frac{EI}{2}(F_{xe}\cos(\theta)+F_{ye}\sin(\theta)+Z)\right)^{\frac{1}{2}} d\theta \tag{A-14}$$

$$U = \frac{EI}{2}\int\left(P\cos(\alpha-\theta)+C\right)^{\frac{1}{2}} d\theta \tag{A-15}$$

Then, applying (A-9) and (A-10):

$$U = \frac{EI}{2}\int\left(P\left((2k^2-1)+\left(1-2k^2\sin^2(\phi)\right)\right)\right)^{\frac{1}{2}} d\theta \tag{A-16}$$

$$U = \frac{EI}{2}\int\left(P\left(2k^2(1-\sin^2(\phi))\right)\right)^{\frac{1}{2}} \frac{2k\cos(\phi)}{\sqrt{1-k^2\sin^2(\phi)}} d\phi \tag{A-16}$$

$$U = EI\sqrt{2P}\int \frac{k^2\left(1-\sin^2(\phi)\right)}{\sqrt{1-k^2\sin^2(\phi)}} d\phi \tag{A-17}$$

$$U = EI\sqrt{2P}\int \frac{k^2-1+1-k^2\sin^2(\phi)}{\sqrt{1-k^2\sin^2(\phi)}} d\phi \tag{A-19}$$

$$U = EI\sqrt{2P}\left((k^2-1)\int \left(1-k^2\sin^2(\phi)\right)^{-\frac{1}{2}} d\phi + \int \left(1-k^2\sin^2(\phi)\right)^{\frac{1}{2}} d\phi \right) \quad \text{(A-20)}$$

This is can then be written using the elliptic integrals in (A-11) as a finite integral from ϕ_1 to ϕ_2 as:

$$U = EI\sqrt{2P}\left((k^2-1)\left(F_e(\phi_2,k)-F_e(\phi_1,k)\right)+\left(E_e(\phi_2,k)-E_e(\phi_1,k)\right)\right) \quad \text{(A-21)}$$

This can be computed directly after solving for *P, k,* ϕ_1, and ϕ_2 in (A-12).

References

[1] B. Tondu and P. Lopez, IEEE Control Syst. Mag. **20**, 15 (2000).

[2] S. Daynes, A. Grisdale, A. Seddon, and R. Trask, Smart Mater. Struct. **23**, 012001 (2014).

[3] E. T. Roche, R. Wohlfarth, J. T. B. Overvelde, N. V. Vasilyev, F. A. Pigula, D. J. Mooney, K. Bertoldi, and C. J. Walsh, Adv. Mater. **26**, 1200 (2014).

[4] J. T. B. Overvelde, T. Kloek, J. J. A. D'haen, and K. Bertoldi, Proc. Natl. Acad. Sci. **112**, 10863 (2015).

[5] D. Yang, L. Jin, R. V. Martinez, K. Bertoldi, G. M. Whitesides, and Z. Suo, Extrem. Mech. Lett. **6**, 1 (2016).

[6] R. D. Beer, R. D. Quinn, Chiel, Hillel J, and R. E. Ritzmann, Commun. ACM **40**, (1997).

[7] S. Collins, A. Ruina, R. Tedrake, and M. Wisse, Science **307**, 1082 (2005).

[8] E. Garcia, M. A. Jimenez, P. G. De Santos, and M. Armada, IEEE Robot. Autom. Mag. **14**, 90 (2007).

[9] T. F. Otero and J. M. Sansinema, Adv. Mater. **10**, 491 (1998).

[10] N. A. Vandesteeg, P. A. Anquetil, P. G. A. Madden, A. Takshi, R. Z. Pytel, S. R. Lafontaine, P. A. Wieringa, and I. W. Hunter, IEEE J. Ocean. Eng **29**, 7006 (2004).

[11] P. Chouinard and J. S. Plante, IEEE/ASME Trans. Mechatronics **17**, 857 (2012).

[12] J. Biggs, K. Danielmeier, J. Hitzbleck, J. Krause, T. Kridl, S. Nowak, E. Orselli, X. Quan, D. Schapeler, W. Sutherland, and J. Wagner, Angew. Chemie - Int. Ed. **52**, 9409 (2013).

[13] R. L. Lieber, *Skeletal Muscle Structure, Function, and Plasticity*, 3rd ed. (Lippincott Williams & Wilkins, Baltimore, USA, 2010).

[14] M. Caruel, J.-M. Allain, and L. Truskinovsky, Phys. Rev. Lett. **110**, 248103 (2013).

[15] C. D. Williams, M. Regnier, and T. L. Daniel, PLoS Comput. Biol. **8**, e1002770 (2012).

[16] G. Piazzesi and V. Lombardi, Biophys. J. **68**, 1966 (1995).

[17] C. D. Williams, M. K. Salcedo, T. C. Irving, M. Regnier, and T. L. Daniel, Proc. R. Soc. B Biol. Sci. **280**, 0697 (2013).

[18] A. M. Gordon, A. F. Huxley, and F. J. Julian, J. Physiol. **184**, 170 (1966).

[19] C. D. Williams, M. Regnier, and T. L. Daniel, PLoS Comput. Biol. **6**, e1001018 (2010).

[20] H. B. da Rocha and L. Truskinovsky, ArXiv Prepr. (2018).

[21] M. Caruel, Mechanics of Fast Force Recovery in Striated Muscles, École Polytechnique, 2011.

[22] R. L. Harne, Z. Wu, and K. W. Wang, J. Mech. Des. **138**, 021402 (2016).

[23] L. Marcucci and L. Truskinovsky, Eur. Phys. J. E. Soft Matter **32**, 411 (2010).

[24] M. Caruel, J.-M. Allain, and L. Truskinovsky, J. Mech. Phys. Solids **76**, 237 (2015).

[25] Z. Wu, R. L. Harne, and K. W. Wang, J. Intell. Mater. Syst. Struct. **27**, 1189 (2016).

[26] M. Epstein and W. Herzog, *Theoretical Models of Skeletal Muscle* (Wiley, New York, USA, 1998).

[27] N. Kidambi, R. L. Harne, and K. W. Wang, Smart Mater. Struct. **26**, 085011 (2017).

[28] J. T. B. Overvelde, S. Shan, and K. Bertoldi, Adv. Mater. **24**, 2337 (2012).

[29] T. Mullin, S. Deschanel, K. Bertoldi, and M. C. Boyce, Phys. Rev. Lett. **99**, 084301 (2007).

[30] K. Bertoldi, P. M. Reis, S. Willshaw, and T. Mullin, Adv. Mater. **22**, 361 (2010).

[31] Smooth-On Inc., (2016).

[32] T. Mullin, S. Willshaw, and F. Box, Soft Matter **9**, 4951 (2013).

[33] ISO, *ISO 37 Rubber, Vulcanized or Thermoplastic — Determination of Tensile Stress-Strain*

Properties (Geneva, CH, 2011).

[34] ISO, *ISO 7743 Rubber, Vulcanized or Thermoplastic — Determination of Compression Stress-Strain Properties* (Geneva, CH, 2017).

[35] R. W. Ogden, *Non-Linear Elastic Deformations* (Dover, New York, USA, 1997).

[36] O. C. Zienkiewicz and R. L. Taylor, *The Finite Element Method*, 5th Editio (Butterworth-Heinemann, Oxford, UK, 2000).

[37] See Supplemental Material at [URL will be inserted by publisher] for video of material state transitions

[38] G. Puglisi and L. Truskinovsky, J. Mech. Phys. Solids **48**, 1 (2000).

[39] T. E. Shoup, An Analytical Investigation of the Large Deflections of Flexible Beam Springs, The Ohio State University, 1969.

[40] T. E. Shoup and C. W. McLarnan, J. Eng. Ind. **93**, 263 (1971).

[41] G. S. Chirikjian, J. Mech. Des. **117**, 573 (1995).

[42] S. Li and K. W. Wang, Smart Mater. Struct. **24**, 105031 (2015).

[43] B. Mosadegh, P. Polygerinos, C. Keplinger, S. Wennstedt, R. F. Shepherd, U. Gupta, J. Shim, K. Bertoldi, C. J. Walsh, and G. M. Whitesides, Adv. Funct. Mater. **24**, 2163 (2014).

[44] R. L. Harne, Z. Deng, and M. J. Dapino, J. Intell. Mater. Syst. Struct. **29**, 265 (2018).

[45] S. P. Timoshenko and J. M. Gere, *Theory of Elastic Stability*, Second (McGraw-Hill, New York, USA, 1963).

[46] J.-S. Chen and Y.-Z. Lin, J. Appl. Mech. **75**, 410241 (2008).

[47] P. F. Byrd and M. D. Friedman, *Handbook of Elliptic Integrals for Engineers and Scientists*, 2nd ed. (Springer-Verlag, Berlin, 1971).